applied sciences

MDPI

Article

Creating a Quasi-Resonant Induction Cooktop Integrating Zero-Voltage Switching (ZVS) and Load Management

Ahmet Aksöz

MOBILERS Group, Sivas Cumhuriyet University, 58140 Sivas, Türkiye; aaksoz@cumhuriyet.edu.tr

Abstract: This study aims to elucidate the development and construction of a durable induction cooktop, with key considerations including efficiency, power customization, and safety features. The intricate processes involved in crafting a 3.5 kW induction burner are thoroughly examined, encompassing simulations for quasi-resonant inverters, the meticulous selection of induction coils and capacitors, the implementation of practical Analog-to-Digital Converter (ADC) filtration, pulse width modulation (PWM) driving techniques, and the integration of protection mechanisms. Leveraging an ARM-based microcontroller enabled the attainment of diverse objectives such as Zero-Voltage Switching (ZVS), safeguarding IGBTs, facilitating user interaction through a user-friendly interface, and enabling load detection capabilities. Furthermore, the capability to gauge and adjust output power based on user preferences was incorporated. Subsequently, rigorous testing was conducted to evaluate the functionality and applicability of the device in real-world scenarios.

Keywords: ARM; ADC; induction cooker; quasi-resonant

check for updates

Citation: Aksöz, A. Creating a Quasi-Resonant Induction Cooktop Integrating Zero-Voltage Switching (ZVS) and Load Management. *Appl. Sci.* **2024**, *14*, 10449. https://doi.org/10.3390/app142210449

Academic Editor: Gerard Ghibaudo

Received: 8 October 2024
Revised: 31 October 2024
Accepted: 1 November 2024
Published: 13 November 2024

1. Introduction

With growing momentum toward full electrification, induction heating presents distinct advantages over traditional methods, excelling in precision, speed, and overall performance. Induction heating (IH) stands as an ideal solution across various applications and industries, from medical devices to diverse hardening and manufacturing processes [1]. Household induction cookers offer a safer, swifter, and more adaptable cooking experience with minimal emissions and independence from natural fuels. It is conceivable that forthcoming government regulations may position domestic induction heating as the preferred solution in the near-future market [2,3].

Recent advancements in modern induction cookers have prioritized safety, user-friendliness, enhanced energy conversion efficiency, and improved power factors. Flexible induction stoves, incorporating arrays of coils, allow users to place cookware anywhere on the surface without concern for positioning [4,5]. Innovative inverter designs employing Zero-Current Switching (ZCS) and Zero-Voltage Switching (ZVS) methods have shown cost and complexity reductions through multi-coil architectures [6]. Further coil reduction strategies, such as the partial overlap proposed by [6], inspired by wireless power transfer gadgets and improved through research on unequal gaps between coils [2], offer promising enhancements.

A novel GaN-HEMT-based inverter introduced in [7] addresses noise and magnetic decoupling issues. Additionally, Power Factor Correction (PFC) rectifiers [8] promise increased efficiency, reduced fabrication costs, and mitigated Electromagnetic Compatibility (EMC) challenges. Enhanced load detection and management solutions, like the one proposed in [9], minimize the need for additional sensors, optimizing power transfer by recognizing pot characteristics. Ref. [3] presents a sensorless safety solution leveraging load material property variations due to temperature changes. Moreover, advancements in cookware design, exemplified by [10], result in improved temperature distribution across loads.

This paper focuses on recent advancements in induction heating systems and quasi-resonant inverters, particularly in induction cooktop designs [11]. Recent innovations have centered on efficiency optimization through improved coil designs, advanced heating materials, and optimized switching frequencies, significantly reducing energy losses. Electromagnetic Compatibility (EMC) remains crucial, with new shielding techniques, active filters, and modulation schemes addressing electromagnetic interference while maintaining performance standards [12–14]. Advanced inverter technologies have seen developments in Zero-Voltage Switching (ZVS) techniques to minimize switching losses, as well as modular multi-level inverter topologies that offer scalability and enhanced power control [15,16]. Additionally, load sensing technologies have emerged, featuring adaptive control algorithms that adjust power output based on load characteristics, thus improving cooking precision and energy efficiency [16]. Noteworthy studies have highlighted dynamic frequency modulation for better load matching and intelligent induction cookers that detect pot sizes and materials, further optimizing heating processes [17].

This paper aims to furnish a practical guide for designing a cost-effective induction burner using quasi-inverter technology, offering insights into circuit design and manufacturing processes. Section 2 introduces fundamental IH principles, followed by an exploration of quasi-resonance inverter workings. Subsequently, limitations and power potential are discussed. Section 3 delves into the key electrical components of an induction cooker, including the inverter circuit and spiral coil. Required peripheral circuits for reliable operation, alongside the microcontroller unit (MCU), are detailed in Section 4. Section 5 addresses safety measures, hard-switching avoidance, and power output control procedures. Finally, Section 6 presents prototype experimentation results compared with theoretical expectations. The experimental results of the proposed solution in this paper subtly underscore the ways in which the proposed solution stands apart from existing commercial alternatives, with the unique aspects of the approach being particularly evident.

2. Quasi-Resonance Circuit

2.1. Principles of Induction Heating

In accordance with Faraday's and Lenz's laws, the introduction of a changing magnetic field in a conductor results in the induction of electrical currents that oppose the original changes in the magnetic field. These circular currents, termed eddy currents [18,19], prompt the material to rapidly heat up upon encountering internal resistance. Illustrated in Figure 1, an alternating current flowing through the red coil produces a variable magnetic field of matching frequency. Guided by a ferrite core and influenced by its shape and penetration depth, this field induces circulating eddy currents within the conductor. In materials exhibiting relatively high resistance, such currents generate significant heat (RI^2), leading to a swift rise in the material's temperature. Additionally, depending on the material type, hysteresis losses [20] stemming from the constant reversal of magnetic fields can further contribute to temperature elevation.

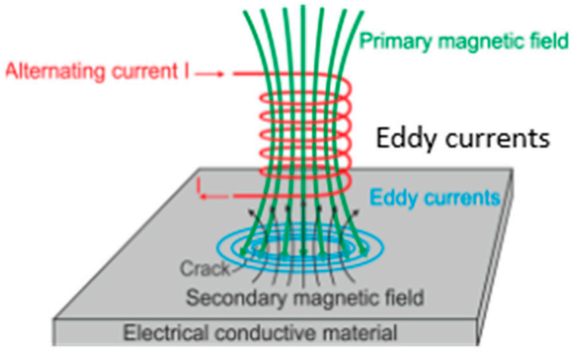

Figure 1. Eddy currents with alternating magnetic fields.

Also, we can determine the penetration depth of the magnetic fields inside the metals by the following [21]:

$$\delta = \sqrt{\frac{\rho}{\mu \pi f}} \tag{1}$$

where ρ, μ, and f denote resistivity [Ω.m], magnetic permeability [H/m], and frequency [Hz], respectively. Equation (1) indicates a reduction in penetration depth as the frequency of the applied magnetic field increases, and therefore, IH provides a distinctive and important feature: the desired depths inside metals can be heated remotely by changing the frequency of the alternating magnetic field [22]. Choosing the right frequency for IH depends on the type of the material, the gap between the piece and the current-carrying coil, the working dimensions, and the desired penetration depth. For example, in induction furnaces for melting different metals, the frequency can range from 50 Hz to 400 kHz (usually, the smaller the object, the shallower the depth of penetration required, so a higher frequency should be used). In our intended application (induction stoves), a working frequency ranging from 25 kHz to 50 kHz can be used [23].

2.2. Operating Principles

Quasi-resonant inverters only require one switching transistor per coil, and they are also sometimes referred to as QR flyback inverters. QR inverters are popular among single-coiled burners and are commonly found in Asian burner markets because of their cost advantage over half-bridge inverters. However, QR inverters have the drawback of not being able to fully control the transferred power to the load, and because of this, their frequency control and EMC issues need to be handled.

It is known that an inductor and a parallel capacitor will exchange energy with each other, and as a result, according to Equation (2), their current and voltage change in a sinusoidal form with a frequency proportional to the capacitance and inductance of the circuit. In Figure 2, for simplicity and a better understanding of how this arrangement works, we consider a situation where the transistor is turned on momentarily only for a short moment and then stays turned off for a very long time (ignoring the effects that the freewheeling diode might have for now).

$$f = \frac{1}{2\pi\sqrt{LC}} \tag{2}$$

where L and C are the inductance [H] and capacitance [F] of the pair, respectively. In a quasi-resonant circuit, when the transistor is turned on, we can assume that the capacitor (C_{res}) quickly gets charged, and the current flowing through the inductor (L_{res}) will rise according to the following:

$$\begin{aligned} V_{bus} &= L\tfrac{\Delta I_L}{\Delta t} \\ I_L &= \tfrac{V_{bus}}{L}\Delta t \end{aligned} \tag{3}$$

Equation (3) reveals that the inductor current grows linearly in time with a slope proportional to $\frac{V_{BUS}}{L}$ (phase I in Figure 2). Then, when the switch (transistor) gets turned off, the inductor and capacitor start to oscillate with each other due to the stored energy in them, in such a way that the current in the inductor will be manifested as the capacitor's voltage. And in the next half cycle, the capacitor voltage transforms into the inductor's current (phase II in Figure 2). Now, in this oscillating state, the energy of the elements involved starts to degrade (due to the internal resistance of the elements) until the oscillation ceases to exist. Our analysis was based on the assumption that we do not consider the freewheel diode, but the fact is, it will start conducting once the inductor current gets reversed and the capacitor is able to match the V_{BUS} (the voltage will eventually surpass $-V_{BUS}$). Then, the inductor's current is no longer being pushed into the capacitor, and until it gets fully depleted, it will pass through the diode and return back to the source (phase III in Figure 2).

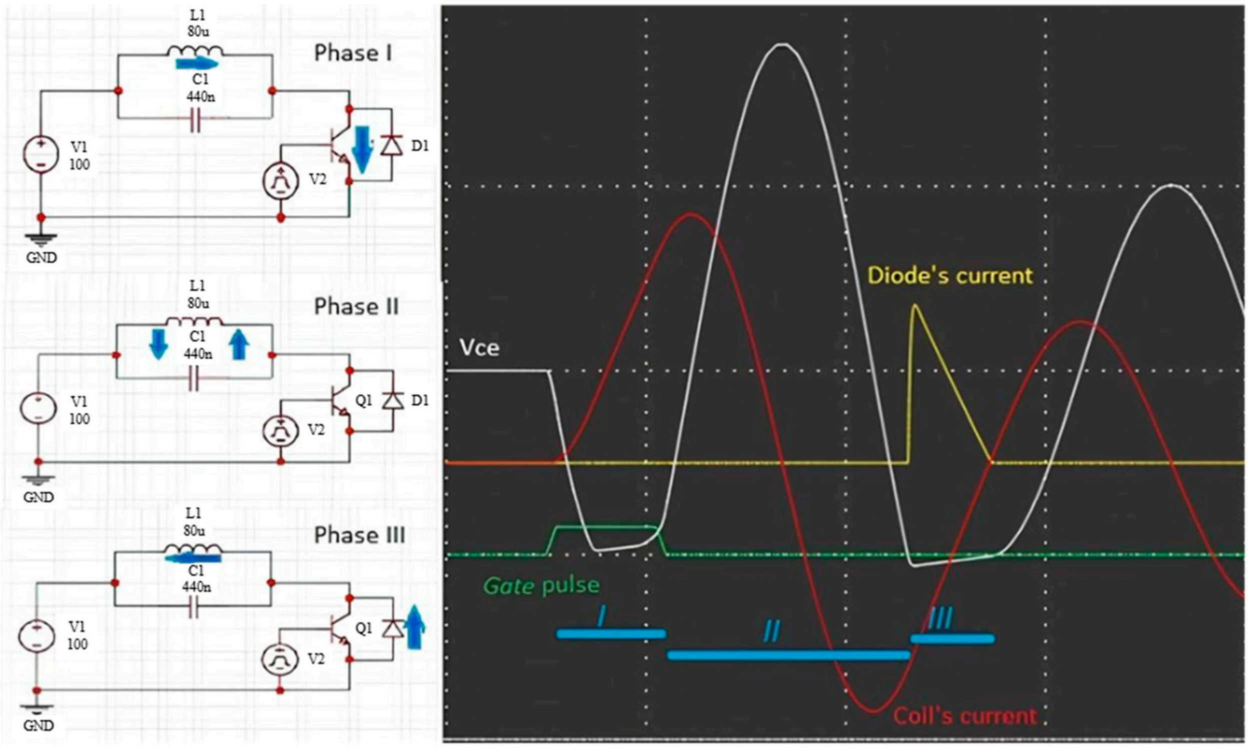

Figure 2. Working basis for quasi-resonant circuit.

Therefore, in short, it can be argued that the system contains only the energy of the capacitor after the first cycle because the energy of the inductor has been discharged in the third phase (Figure 2) [24]. This means the majority of the energy transfer takes place only in the first cycle after switching, so theoretically, with the start of the second cycle, switching can be initiated once again [25].

2.3. Constraints

In Figure 3a, before switching the transistor, V_{BUS} is placed across the collector–emitter junction of the transistor (V_{CE}), and when it gets turned on (moment 1 in Figure 3b), the current of the inductor increases linearly with time (according to Equation (3)), and when the switching stops, the oscillation between the inductor and the capacitor causes the energy of the inductor to be stored in the form of capacitor voltage. Depending on its polarity, this voltage can inflate V_{CE} (moment 2) or reduce it to the point of the reverse conduction threshold at which the freewheeling diode gets activated (moment 3). After that, the circuit continues to oscillate with the energy that has been left in the capacitor (in Figure 3b, the difference between the peak voltages of the first period and the subsequent ones indicates an energy discharge during the diode conduction phase).

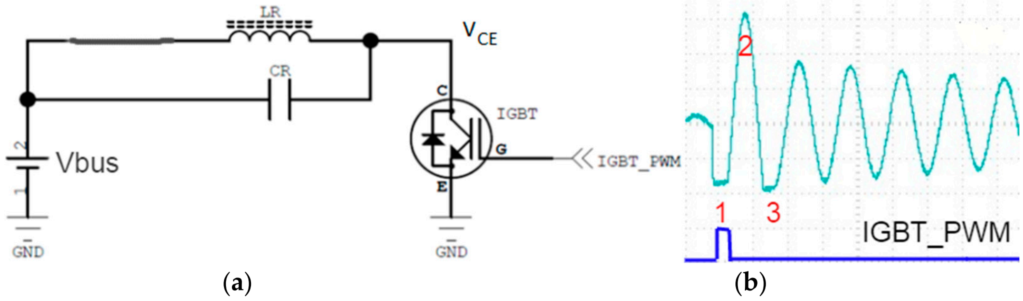

Figure 3. Transistor voltage during circuit excitation (**a**) circuit (**b**) IGBT PWM output.

In Figure 3, moment 2 is the maximum voltage that the transistor will experience, and we can express it as the sum of the source voltage (V_{BUS}) and the capacitor voltage ($V_{C,max}$), since the total energy of the system, including the capacitor and inductor, is cumulated solely in the capacitor.

$$\begin{gathered} E_L = \tfrac{1}{2}LI_L^2 \\ E_C = \tfrac{1}{2}CV_C^2 \end{gathered} \tag{4}$$

$$E_C[\max] + 0 = E_C[t] + E_L[t] \tag{5}$$

Equation (5) shows that, at this particular moment, the energy of the system is completely stored in the capacitor and is equal to the sum of the energy from the inductor and the capacitor, at all times (only the first cycle is considered here). Since their energy at moment 1 is known according to the following equations, the maximum voltage of the capacitor can be calculated:

$$I_L = \frac{V_{bus}}{L}\Delta t, V_C = V_{bus} \tag{6}$$

$$\begin{aligned} \tfrac{1}{2}CV_{C,\max}^2 &= \tfrac{1}{2}CV_{bus}^2 + \tfrac{1}{2}L\left(\tfrac{V_{bus}}{L}\Delta t\right)^2 \\ V_{C,\max} &= \sqrt{\frac{L\left(\frac{V_{bus}}{L}\Delta t\right)^2 + CV_{bus}^2}{C}} \\ V_{CE,IGBT} &= \sqrt{\frac{L\left(\frac{V_{bus}}{L}\Delta t\right)^2 + CV_{bus}^2}{C}} + V_{bus} \end{aligned} \tag{7}$$

In the above equations, Δt denotes the time period in which the transistor is conducting and charging the inductor [Sec]. The obtained formula expresses a direct relation between the transistor's maximum voltage (during switching) with Δt. And if it exceeds more than the permissible limit, it will lead to permanent damage to the transistor.

The transferred induction power can be assessed by considering one switching cycle of the transistor. During this time, the energy is conveyed from the source to the inductor, which is then absorbed by the metallic load during oscillation. This statement heavily relies on the condition that the coil winding and the metallic recipient form a decent enough imperfect transformer [26,27]. This means that all the magnetism produced by the primary coil gets lost in the core, which is of course our desired purpose in induction heating since it will maximize the magnetic engagement between the coil and the load. In induction heating systems, the transistor functions as a crucial switching element that controls the flow of current to the inductor. The time period Δt during which the transistor is in a conductive state is essential because it directly affects how much energy is transferred from the power source to the inductor. During this conduction phase, the inductor accumulates energy in the form of a magnetic field. The relationship between the maximum voltage across the transistor, VCE, max, during switching and Δt is critical; if the maximum voltage exceeds the transistor's breakdown voltage, which is the highest voltage the transistor can withstand without failure, it can result in irreversible damage. Therefore, effectively managing Δt is vital for ensuring the reliability and longevity of the device. Therefore, according to this ideal assumption, we can conclude the following:

$$W = \frac{\frac{1}{2}LI_L^2 + \frac{1}{2}CV_C^2}{T_{on} + T_{off}} \tag{8}$$

To fully understand the energy transfer process in an induction heating system, one must consider a complete switching cycle of the transistor. During this cycle, energy flows from the source to the inductor while the transistor is conducting. Once the transistor turns off, the energy stored in the inductor is released and subsequently transferred to the load (usually a metallic object) during the oscillation phase. This transfer mechanism is central to achieving efficient induction heating. The effectiveness of this energy transfer is significantly influenced by the coupling between the coil winding (the primary side) and the metallic load (the secondary side). For optimal performance, the system is designed to function as an "imperfect transformer", allowing a considerable amount of the magnetic flux generated by the primary coil to interact effectively with the load, maximizing energy transfer. In the above equation, T_{on} is the same as Δt, and T_{off} is the time taken for a complete energy transfer to load, which, with a good approximation, the oscillation period can be substituted for. Also, as we will show later, during the operation of the system, the energy of the inductor is much higher than the energy of the capacitor, and therefore, by ignoring it, and with the help of Equation (3), the above can be rewritten and simplified as follows:

$$W = \frac{\frac{1}{2}L\left(\frac{V_{bus}}{L}\Delta t\right)^2}{T_{on} + T_{res}} \tag{9}$$

Equation (9) takes this analysis a step further by simplifying the relationship by neglecting the energy contribution from the capacitor. In many high-frequency applications, the energy stored in the inductor often far exceeds that of the capacitor, making it a dominant factor in the system's energy dynamics. This simplification allows for a clearer understanding of the system's performance without the additional complexity introduced by the capacitor's behavior. Based on Equations (7) and (9), the $V_{CE,max}$ of the transistor is limited by Δt, but on the other hand, the power is directly increased by raising Δt, so the maximum power that the device can transfer is limited by the breakdown voltage of the transistor. For instance, if the breakdown voltage is considered to be 1200 V and V_{BUS} = 220 V, then by introducing C = 440 nF and L = 80 μH, for the maximum power, the device can roughly handle 3.5 kW [21].

$$\begin{gathered} V_{V,\mathrm{max}} + 220V = 1200V \\ \sqrt{\frac{L\left(\frac{V_{bus}}{L}\Delta t\right)^2 + CV_{bus}^2}{C}} = 980V \\ \Delta t_{\mathrm{max}} = 25ms \rightarrow W_{\mathrm{max}} \approx 3.5kW \end{gathered} \tag{10}$$

The breakdown voltage of the transistor is a critical parameter that dictates the operational limits of the system. If the VCE, max surpasses this threshold, it may lead to transistor failure. Consequently, effective power management becomes essential. While increasing Δt can enhance the energy transferred to the load, the maximum power that can be handled by the system is constrained by the breakdown voltage of the transistor.

3. System Design in Component Level

The electrical elements of the system, such as the inverter and coil, should be designed so that, in addition to the appropriate dimensions of the coil, the inductance variation after placing the load is not too severe. In [10], cookware enhancements are shown to deliver a uniform temperature across the workpiece. Induction burners usually operate at frequencies between 25 kHz and 30 kHz for switching so that the requirements for the penetration depth and inaudibility of the device can be met.

According to Equation (2), by choosing 27 kHz for the no-load oscillation frequency and fixing the appropriate dimensions of the coil, an inductance value of 76 μH for the coil and capacitance of 440 nF for the capacitor are chosen. The durability of the capacitors in handling high voltages along with temperature swings should be considered during the selection process, since when the energy of the inductor is transferred to the capacitor, it will cause a great surge in the capacitor's voltage. Another factor worth mentioning is that during the heavy operation of the inverter, the current constantly fluctuates between the inductor and capacitor, thus causing the capacitor to heat up. Therefore, film capacitors with polyester dielectric or polypropylene are selected [28,29].

In induction stoves, the ferrite cores under the main coil provide a low-reluctance path for the magnetic field, thus acting as a shield so that the magnetic flux can be concentrated on the load above. By neglecting their effect on the net inductance, we consider only the coil itself for now. In [6], the use of overlapped coils is discussed, which allows for a flexible working surface and simplicity of production. Generally, induction cooker coils comprise spiral, flat windings [30]. To calculate the inductance of such a coil, parameters such as the wire diameter, number of turns, distance between wires, and inner radius are introduced to the existing calculators [31]. A good estimation for making a viable coil is a 12 m long wire with a 2 mm diameter. High-copper alloys should be used in fabrication, since copper is not considered a suitable host for eddy currents due to its low electrical resistance. Figure 4 shows that the inductance measurement of the coil by the LCR meter is manifested. As can be seen, there is little difference between the theoretical and practical values [32].

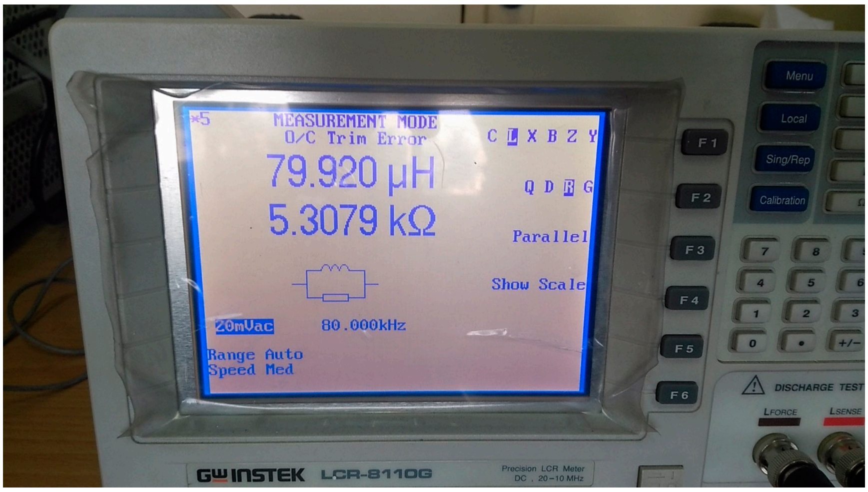

Figure 4. Coil's inductance measurement.

Due to heavy noise in the inverter, during switching and rapid capacitor charge, IGBTs are a better choice since MOSFETs are more sensitive to momentary changes in the working voltage, which can cause them to get damaged. IGBTs, on the other hand, are more tolerant of these changes and are therefore less likely to be damaged. Additionally, IGBTs have higher current ratings, which means that they can deliver more power. The STGWT20IH125DF IGBT from STMicroelectronics, with a breakdown threshold voltage of 1200 Volts and a current rating of 15 Amperes, was chosen due to its suitable price and heat tolerance [33].

4. Peripheral Circuits

For feasible IGBT switching, the PWM signal from the microcontroller must be amplified and be able to supply enough current to the gate to ensure the transistor's smooth operation. Also, without proper isolation, the high voltages in the inverter will make their way into the electronic circuits. In this case, the possible damage will be irreparable. For this reason, the TLP250 chip [34] was used, as shown in Figure 5. The TLP250 chip is an opto-electronic power driver with internal isolation capabilities [35].

In Figure 6 part 1, the voltages across the two ends of the coil and capacitor are reduced by a resistor pair and fed to the op-amp in part 2. Because the designed circuit is not functioning in feedback mode, the output of the op-amp (PULSE-DET) will also change along with the oscillation, as shown in Figure 7 (blue waveform). Therefore, by observing the PULSE-DET signal, it is possible to confirm the presence of the load on the coil.

The LM324 chip has four operational amplifiers inside of it, which are used here to sample collector–emitter voltage fluctuations and the IGBT current and detect the critical temperature of the heatsink on which the IGBT is mounted. For the sake of simplicity, the design circuitry is divided into five sections in Figure 7. In the following, their utilization will be briefly discussed.

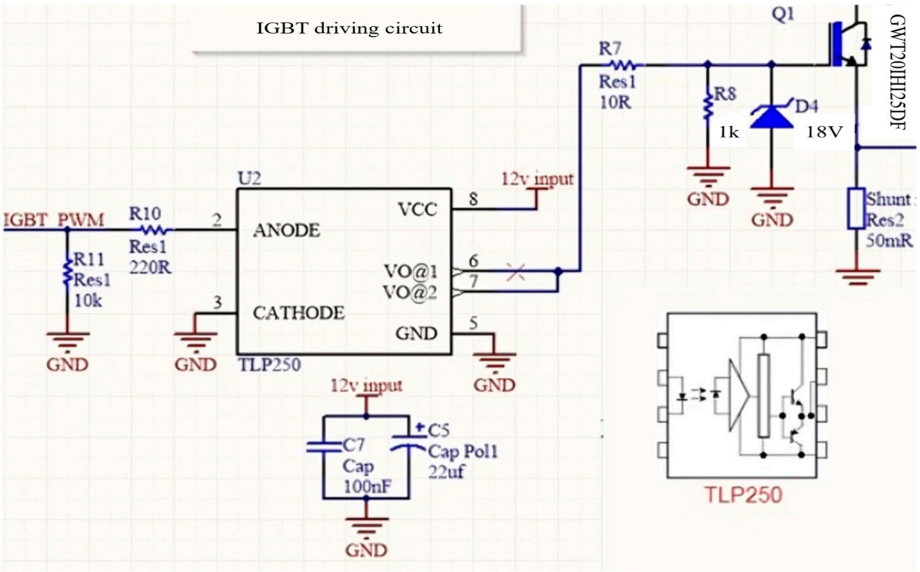

Figure 5. IGBT driving circuit.

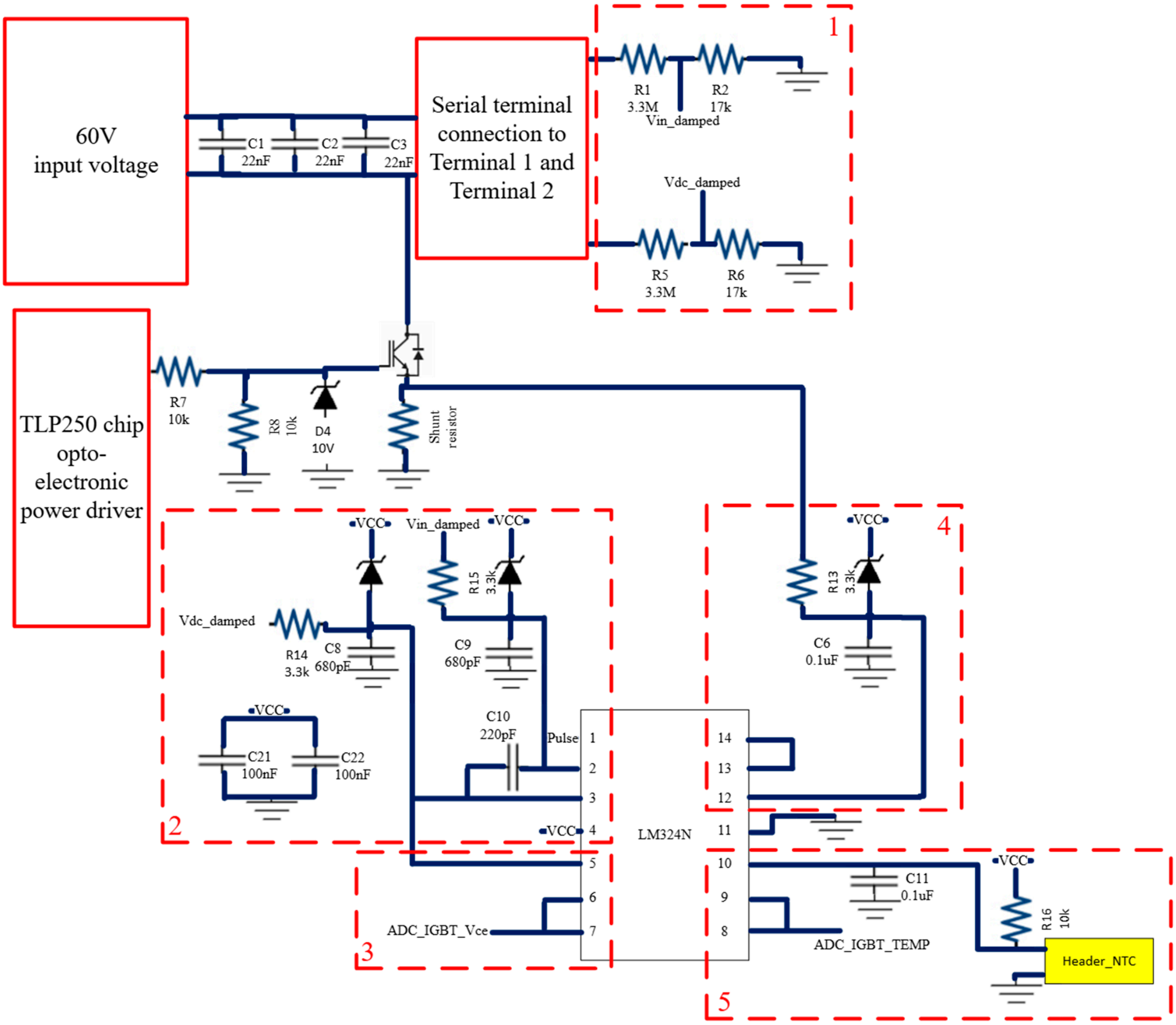

Figure 6. Measurement circuits.

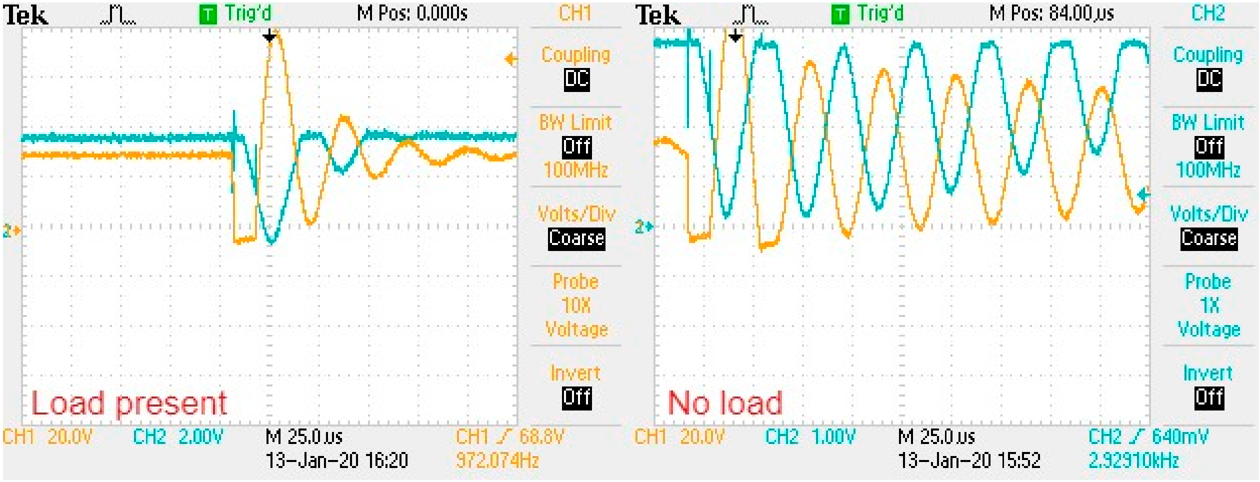

(**a**) (**b**)

Figure 7. Resonating voltage. (**a**) Load is present. (**b**) Without load.

During the excitation of the coil (transistor switching), the operation condition can be categorized into two types based on the oscillation that takes place. According to Figure 7, if there is a load present on the coil (a), the oscillation voltage (shown in orange) is damped out in the first few periods. However, if there is no load present (b), the oscillation continues. Therefore, this feature can be used to ensure the existence of the load on the coil.

The resistors and capacitors in part 2 provide sufficient filtering for the VIN_DAMP and VC_DAMP voltages. For example, capacitor C8 and resistor R14 form a low-pass filter with a specific frequency cutoff of $f = \frac{1}{5.R.C} \approx 90$ kHz. This removes upper disturbing frequency harmonics from VC_DAMP. Zener diodes D6 and D7 protect the op-amp input in the case of an overvoltage surge [36]. In Figure 6 part 3, VC_DAMP (IGBT collector–emitter voltage) is an input signal for the op-amp, which in this case acts as a follower; then, the op-amp output (ADC_IGBT_VCE) is sent to the microcontroller for further processing. Also, an NTC resistor (Figure 8) is placed on the heatsink, which is used to secure the temperature of the transistor and protect it against overload.

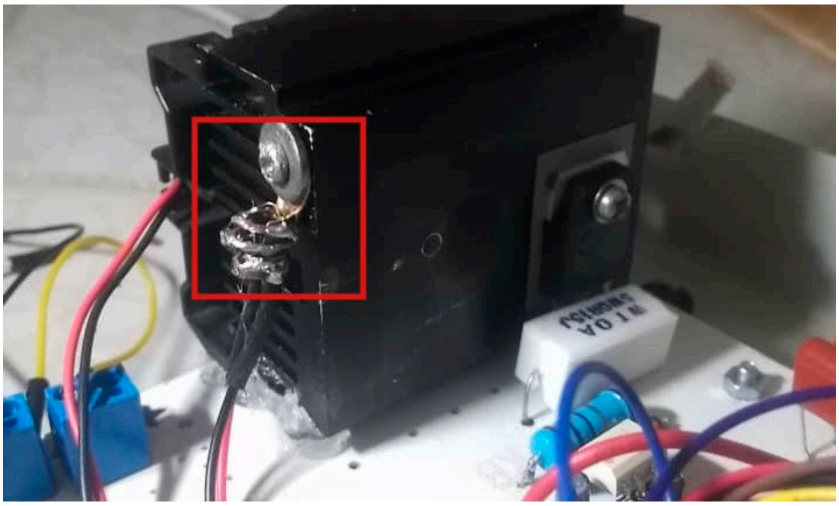

Figure 8. IGBT heatsink and its NTC.

Measuring the system's current is necessary to calculate the output power. Therefore, a 150 mΩ shunt resistor (wire-wound resistor in front of the IGBT in Figure 8) is introduced to the circuit. The derived voltage as a result of the current passing through it is filtered by a conjunction of C6 and R13 (Figure 6 part 4). Therefore, it can be assured that the

ADC_IGBT_CURRENT signal correlates with the average current of the system. This signal is also passed to the MCU for sampling.

5. Microcontroller

The STM32F103C8T6 microcontroller [37] is used as the main control unit of the device. It includes a Cortex-M3 processing core from ARM technology, along with 64 kb of flash memory, a working frequency of 72 MHz, 37 I/O ports, UART, USB, SPI, I2C communication, DAC and ADC converters, timers, and many other peripherals that meet the requirements for mid-range systems. Figure 9 depicts the program's flowchart for the MCU code. In this section, we try to mention the most important divisions of the program and avoid the details of the implementation as much as possible. We have divided the program into five modules, and we will discuss each of them in the following.

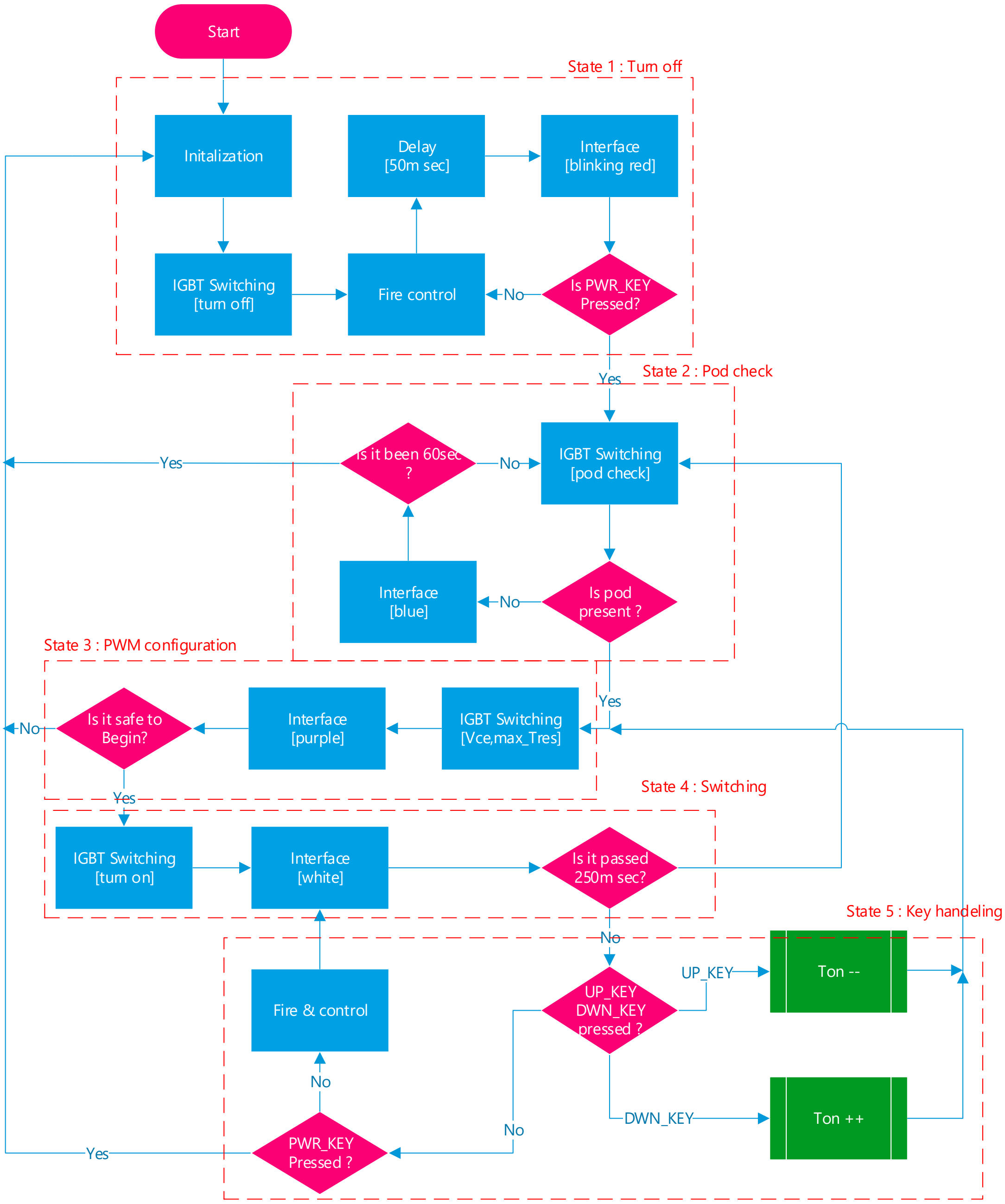

Figure 9. Flowchart of the main program.

5.1. Flowchart

Although the selected transistor has a breaking threshold of 1200 volts, Δt cannot be incremented too much because of the 600 V practical limit on the capacitor's working voltage. Additionally, when the switching takes place, the coil's drawn current escalates quickly, and it is important to validate the power source's ability to provide the demanded current. Therefore, we have designed the system in such a way that Δt increases gradually so that in case of error detection, the system can catch up and act properly. The flowchart includes the following:

(1) Standby: When the device is turned on, the initialization block performs the initial settings of program variables and HAL-related handlers. The IGBT switching block disables PWM generation (transistor shutdown); then, a routine updates the LEDs and the display module, putting the device in red flashing mode. Consequently, the program waits for the user to press the power key (PWR_KEY).

(2) Load check: The IGBT switching block is used to detect the presence of cookware on the coil [38–41]. If it does not perceive any magnetic engagement due to the presence of the load within 60 s, the program will return to its previous state. Additionally, in this mode, the LED will be changed to blue.

(3) PWM configuration: After detecting the load, it is time to determine the switching parameters. At this stage, $V_{CE\text{‹}max}$, $T_{resonance}$, and Δt_{on} will be determined by triggering pulses at low frequencies to excite the coil.

(4) Switching: In this step, the PWM pulse generation process is started by the IGBT switching unit. At the same time, a routine continuously checks the safety parameters such as the IGBT temperature, current, power, etc. To ensure the presence of the load (container), the system returns to load detection (module 2) every 250 milliseconds. This time, the system will not require confirmation from the user. The display LED will be white in this state.

(5) User interface: Normally, when the device is in the operating state, it will loop around module 4. However, pressing any of the following keys, PWR, UP, and DWN, will execute module 5. Pressing the UP_KEY button will increment Δt, which will increase the total output power. On the contrary, pressing the DWN_KEY button will decrease Δt, which will decrease the total output power. The PWR_KEY button also shuts down the system. After this step, the program will go to step 3 and then return to the main module (switching state) after determining the new PWM specifications.

The fire control block is implemented to monitor the state of the transistor during switching and estimate the output power. This block keeps track of the IGBT temperature and system current by sampling the ADC_IGBT_TEMP and ADC_IGBT_CURR signals (in the ADC1 unit). Then, by comparing the values to pre-defined limits, it controls the heatsink fan (IGBT_FAN) and shuts down the system if the temperature exceeds the critical level. Also, with the help of the measured current, the real-time power value is stored in the SYSTEM_POWER variable to be displayed on the screen using the interface block. In the microcontroller, timer 3 is responsible for generating the PWM needed to switch the IGBT. This block transfers the pulse to the corresponding IGBT_PWM port, which is then used to drive the IGBT using TLP250. The switching parameters can be managed as follows:

$$\begin{aligned} TIM3\_ARR &= \Delta t_{on} + T_{off} \\ TIM3\_CCR1 &= T_{off} \end{aligned} \tag{11}$$

For example, Figure 10 shows a PWM pulse with a Δt period of 5 microseconds and a period of 35 microseconds. Consequently, if we need to increase the power, we will modify the registers accordingly.

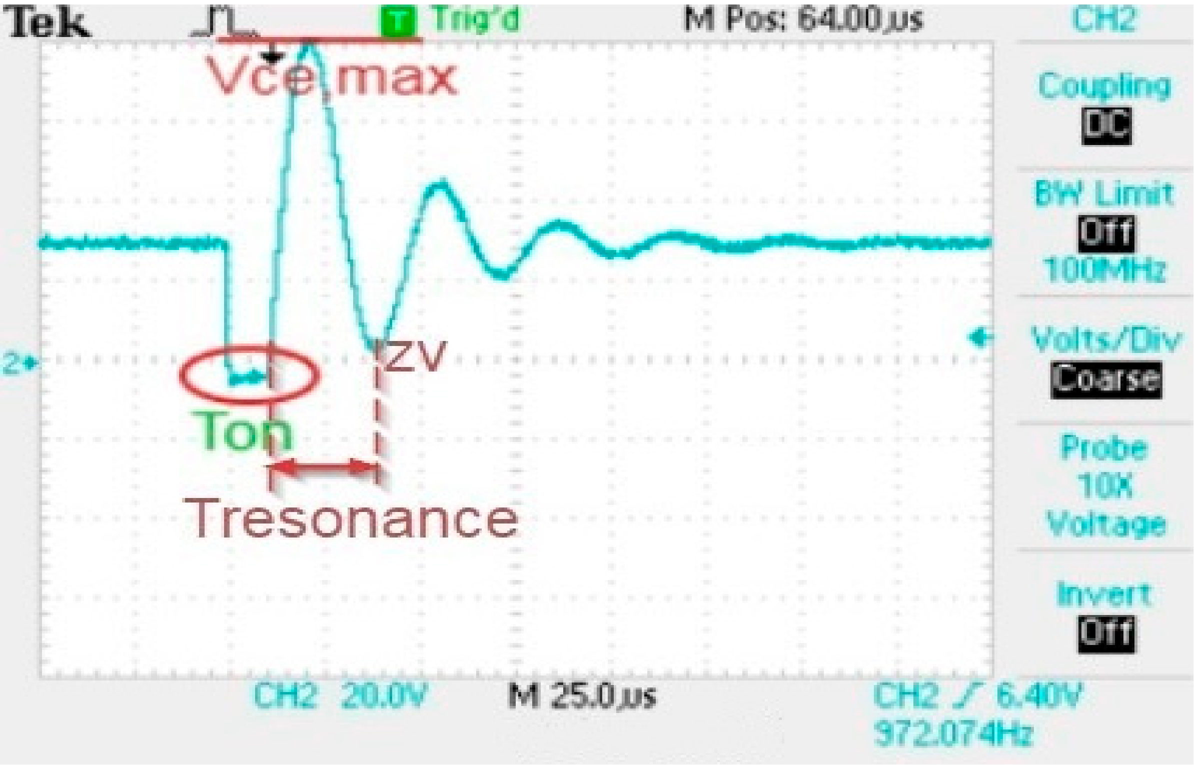

Figure 10. ZVS parameters.

By intermittently exciting the coil, we can detect the presence of the load by counting the periods of the PULSE_DET signal. For this purpose, the PULSE_DET signal is placed in the timer 2 unit with the Capture input mode, and its changes are measured right after the transistor turns off (circuit oscillation begins). Ref. [9] suggests an interesting deep learning solution for material identification. A practical test determined that if this value is more than three oscillation periods, there is no proper flux interaction between the coil and the pot [41–45].

5.2. ZVS Detection

The transistor losses can be greatly reduced if the switching is timed correctly. This method is known as Zero-Voltage Switching (ZVS). In ZVS, the transistor's voltage fluctuation is monitored, and the turn-on pulse is not applied until the collector–emitter voltage reaches zero. This causes the transistor to operate in a soft-switching area, and therefore, the losses due to switching are significantly reduced. As discussed earlier, in a quasi-resonant inverter, applying ZVS methods is like swinging a pendulum at the right time, as it requires precise real-time information about the system's condition. Ref. [4] proposes a novel multi-coil ZVS inverter that can be used in flexible surface induction cookers.

This feature is implemented in the MCU's program, and T_{off} is calculated by designing an algorithm that measures the blackout time needed for V_{CE} to reach zero. Since the flux interaction between the coil and the load often changes with displacement on the coil or the use of different materials, the presumed oscillation frequency is no longer constant and must be calculated periodically. It is also noteworthy that the oscillation period of the system is slightly different from T_{off}.

The algorithm is written in such a way that after the coil is briefly energized with specific periods (T_{on} in Figure 11), the ADC_IGBT_VCE signal (IGBT voltage) is sampled regularly by the ADC2 unit; then, by applying the differential analysis, the point of ZVS (zv in Figure 11) is determined. After that, T_{off} gets calculated, and the highest V_{CE} value is recorded for the given Δt_{on} (which should not surpass the rated voltages).

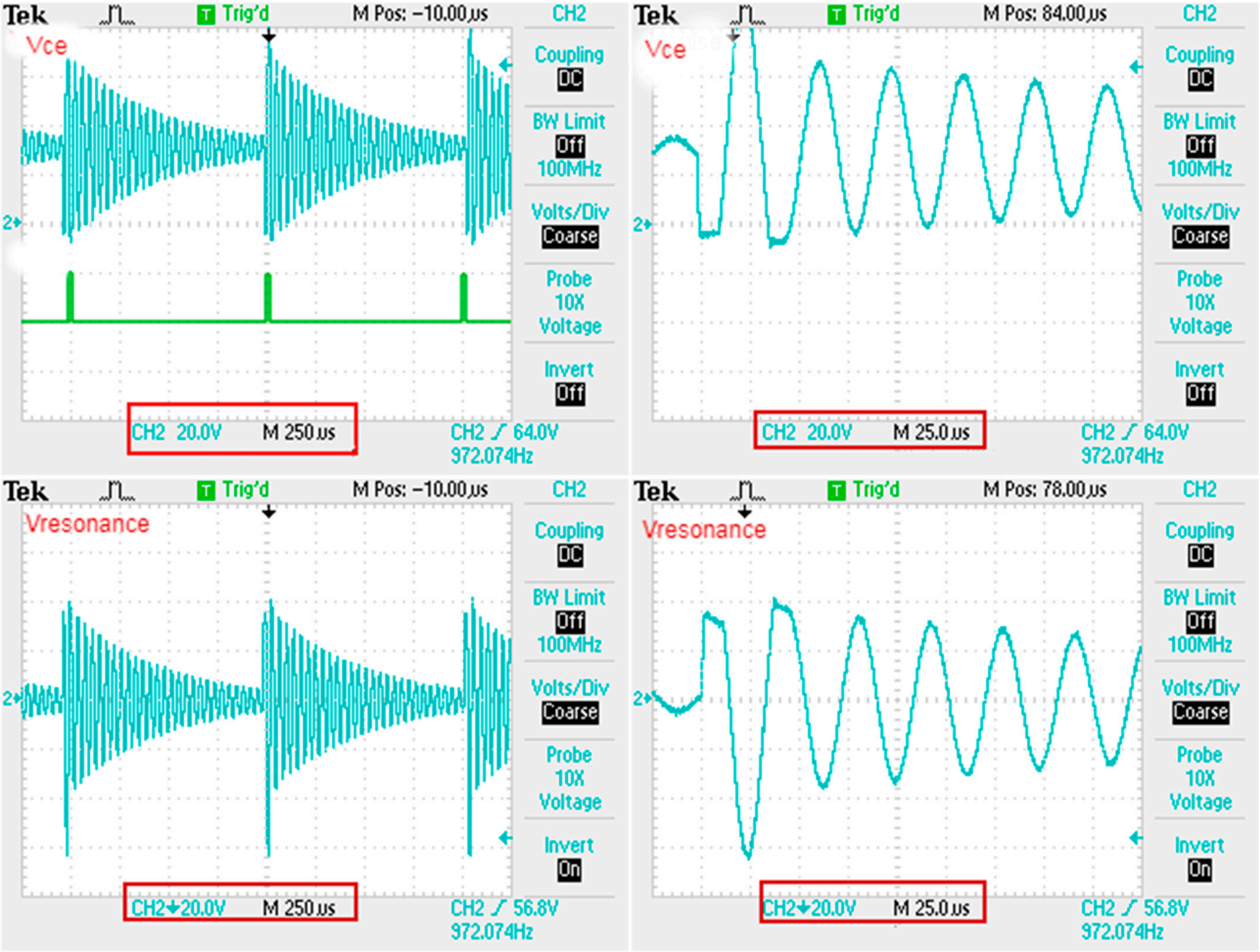

Figure 11. Low switching frequency (no load).

6. Prototype Test

An adequate power supply was used to provide 30 Volts to the switching line (V_{bus}). Then, the voltage variation and other control signals were observed and measured using a digital oscilloscope in the laboratory. The results are discussed below.

6.1. Load-Free Test

At first, we observed the transistor's V_{CE} and the coil oscillation voltages without any load, with specifications of $T_{off} = 1000$ µs and $\Delta t_{on} = 10$ µs. Figure 11 displays the results on the oscilloscope (the IGBT start-up pulse appears in green). In Figure 11, the maximum collector–emitter voltage is observed during the first period after the energizing pulse. This voltage must be managed for each Δt_{on} (pay attention to the 90 V peak of the collector–emitter voltage). In the second part, we will switch the transistor at a higher frequency with the specifications of $T_{off} = 24$ µs and $\Delta t_{on} = 20$ µs. The resulting waveform can be seen in Figure 12.

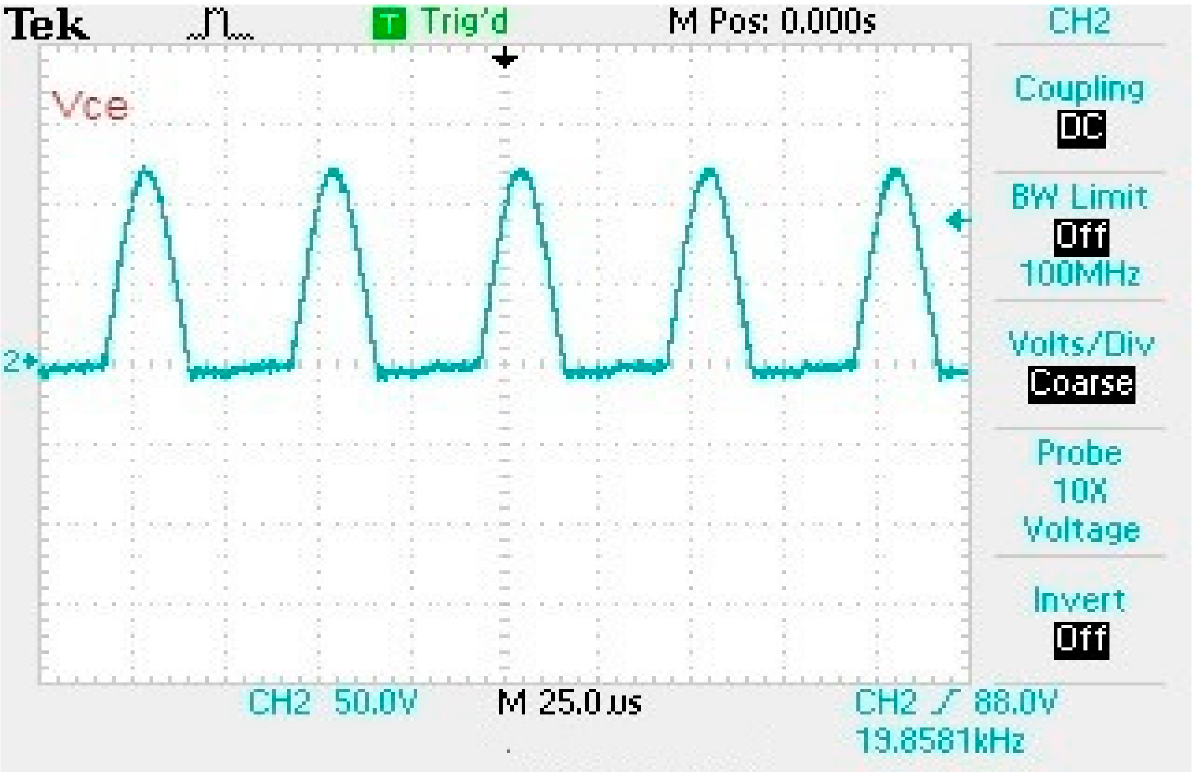

Figure 12. ZVS.

Here, we resume switching just before the second cycle of oscillation is about to begin. As expected, the maximum voltage of the transistor increases to 125 Volts. The above waveform indicates that the device is operating in an optimal state, as the collector–emitter voltage reaches zero after the inductor's energy is depleted by the freewheel diode. This is the ideal moment for the ZVS of the system. Therefore, we can also confirm that our ZVS algorithm correctly predicted the value of the needed T_{off}.

6.2. Loaded Test

The previous test is repeated by placing an iron pot on the coil and observing the resulting waveforms, shown in Figure 13. It can be seen that after a few cycles (after which the transistor is no longer conducting), the system stops oscillating due to energy being transferred to the load. The collector–emitter peak voltage decreases slightly but not significantly. It is still important to monitor $V_{CE,max}$ and adjust Δt_{on} accordingly.

Next, we observe the behavior of the system when the switching parameters are changed back to the previous no-load conditions ($T_{off} = 24$ µs, $\Delta t_{on} = 20$ µs). It can be seen that the system is no longer operating in ZVS, as the T_{off} changes because of inductance variation due to the load being present. Therefore, it is essential to use the mentioned algorithm to predict the correct switching time for the optimal operation of the device. (In Figure 14, the orange waveform shows V_{CE}, and the blue one represents the IGBT_CURR signal.)

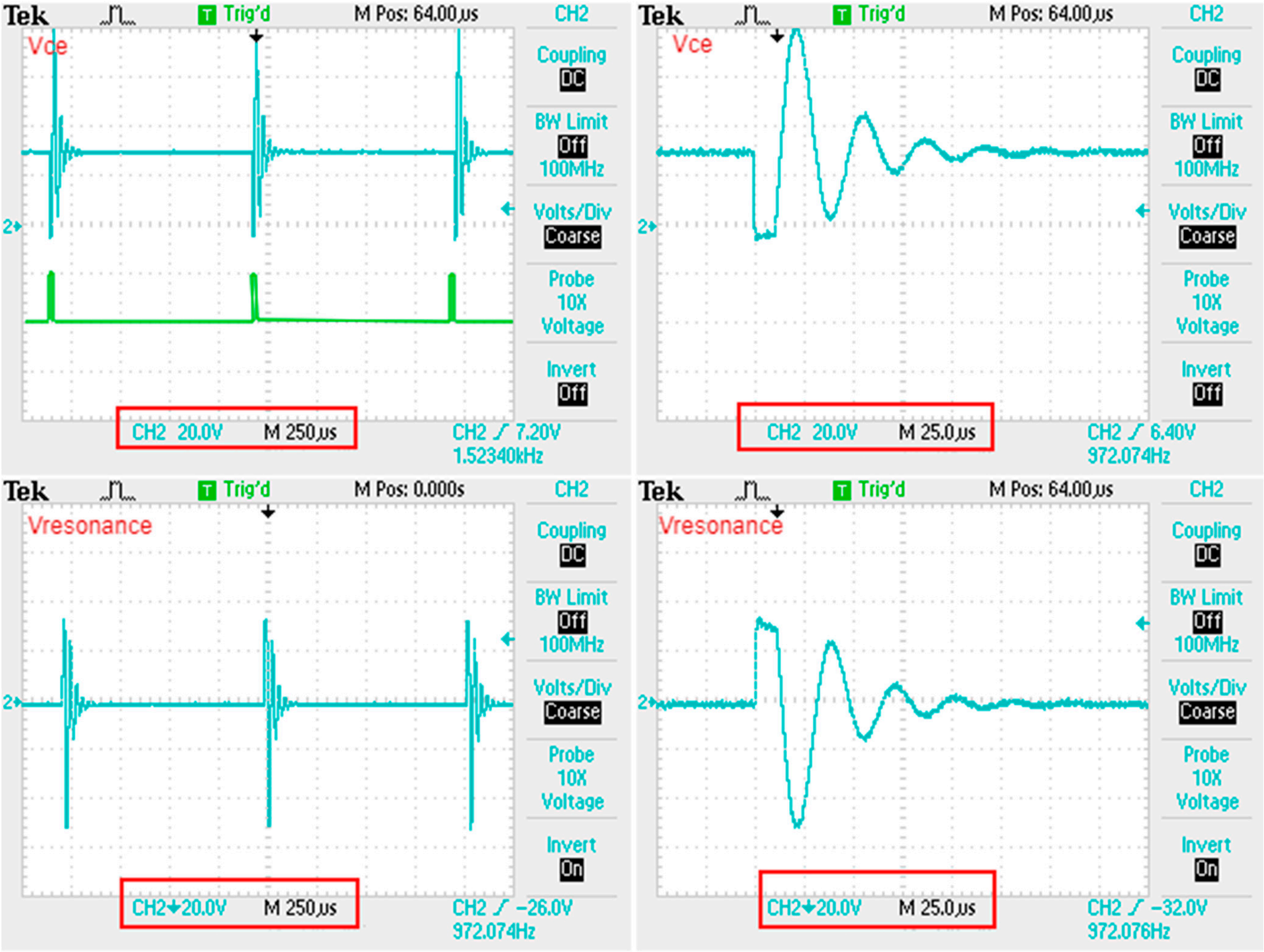

Figure 13. Low switching frequency (with load).

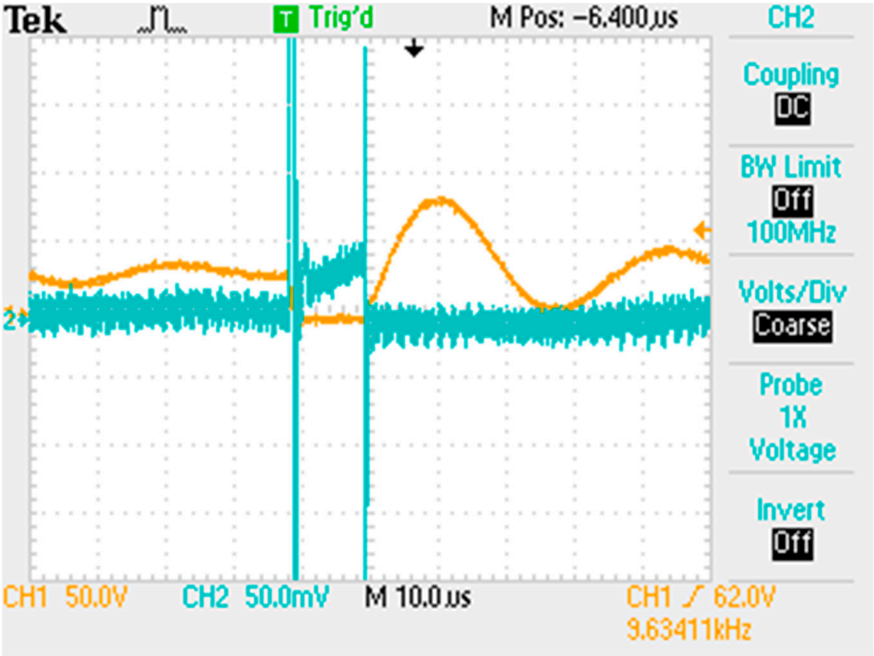

Figure 14. Switching with load.

6.3. Comparison

Table 1 shows that there is a direct relationship between Δt_{on} and the critical voltage of $V_{CE,max}$, as mentioned in Equations (7) and (10), for the inverter. Additionally, the measured waveforms clearly show the importance of the applied ZVS technique, as it prevented the additional stress and losses caused by switching.

Table 1. IGBT critical voltage based on switching parameters.

Figure	$\Delta t_{on}(\mu s)$	$T_{off}(\mu s)$	$V_{CE,peak}(V)$	Load
12	10	1000	90	Without
14	10	100	80	Present
13	20	24	125	Without
15	20	24	120	Present

In addition, the equipment and components used to ensure and emphasize the repeatability and sustainability of this study are given in Table 2. Here, the details are kept confidential so as not to hinder future studies and for the patent application process. However, this information will be sufficient for researchers working on this subject because the original point here is the designed circuit and control software.

Table 2. Setup equipment and components.

Category	Equipment/Components
Quasi-resonant inverter	Power MOSFETs and/or IGBTs Inductor and capacitor components for the resonant circuit Diodes for rectification
Microcontroller unit (MCU)	STM32 microcontroller Development board for STM32
Control system components	Shunt resistors for current sensing NTC thermistors for temperature monitoring Voltage measurement circuits (operational amplifiers for scaling)
Power supply	Adjustable DC power supply for inverter testing
Load testing equipment	Resistive load bank or induction heating load
Measurement instruments	Oscilloscope for monitoring voltage and current waveforms Digital multimeter for voltage and current measurements Temperature measurement system (digital thermometer and data logger)
Calibration equipment	Calibration sources for voltage and current Calibration standards for temperature sensors
Prototyping tools	Breadboard and PCBs for circuit assembly Soldering equipment and tools for circuit assembly and modifications
Safety equipment	Insulation resistance tester Thermal imaging camera or infrared thermometer for safety checks Fume hood or ventilation for testing potentially hazardous components

To evaluate the feasibility and real operation of our prototype, we increased the input voltage of the device to 60 V by connecting two 30 V power sources in series, as shown in Figure 15. Then, we placed an iron piece on the spiral coil and observed the temperature changes as follows.

Figure 15. Heating a metallic disk.

Once the device was turned on, we measured the temperature of the iron disk using a laser thermometer. As shown in Figure 16, the temperature of the iron piece increased by 34 degrees. The device also displayed the power of the system as 112 W, which accurately corresponds to the voltage and current drawn from the source. When the piece was removed from the coil, the device stopped, and the status indicator light turned blue, which indicates that the load presence procedure functioned correctly when the load was removed from the system.

Figure 16. Temperature measurement.

In the results shown in Sections 6.1 and 6.2, an academic study was carried out, especially focused on the thermal values of the laboratory setup, and the electrical efficiency of the proposed method is shown with successful results in parallel with the given literature examples. The output that should be mentioned here is the efficient result values in the loaded and unloaded results of the method used, and this is a result independent of the heater being next to it. Figures 15 and 16 are given only to visually enrich the visuals of the heating and measurement values of the system.

However, magnetic losses in ferrite cores are critical factors affecting the efficiency and performance of high-frequency devices, such as induction cooktops. These losses consist mainly of hysteresis losses, which arise from the magnetization and demagnetization of the core material as the magnetic field fluctuates, and eddy current losses, which result from circulating currents induced within the core due to changing magnetic fields. The Revised Generalized Steinmetz Model (RGSM) offers a robust framework for estimating these magnetic losses under varying operating conditions. The RGSM expresses core losses Pcore as a function of the peak flux density B and frequency f using the equation $P_{core} = k.B^x.f^y$, where k, x, and y are material-specific coefficients determined empirically. This model provides a more accurate representation of core losses by considering the complex interactions between frequency and flux density, making it particularly relevant for high-frequency applications [46–48]. By employing the RGSM, the core performance can be predicted more accurately, design parameters can be optimized, and suitable ferrite materials can be selected, ultimately leading to more efficient induction heating systems. Understanding these losses is crucial for enhancing device reliability and longevity, ensuring that modern applications meet their efficiency demands.

7. Conclusions

This study thoroughly explored the utilization of a quasi-resonant inverter in the development of an induction cooker, carefully considering critical factors such as circuit limitations, load detection mechanisms, and durability requirements to optimize the device's performance. The analysis provided a detailed overview of the simulation and implementation of the quasi-resonant inverter (QC inverter), highlighting its role in achieving efficient power transfer and stable operation. A significant portion of the research focused on the control system architecture, with an in-depth explanation of the flowchart program designed for the STM32 microcontroller (MCU), which governed the system's key processes. The control scheme included the precise management of peripheral circuits essential for the system's operation, such as shunt resistors used for current sensing, NTC thermistors for real-time temperature monitoring, and voltage measurement circuits to ensure accurate feedback control. Each component played a vital role in maintaining the cooker's safety and functionality, with algorithms tailored to detect load conditions and adjust power levels accordingly. Additionally, this research delved into the calibration procedures for temperature and voltage sensors to enhance the reliability of measurements under varying operational conditions.

This study did not stop at theoretical modeling and simulations; it extended to practical implementation, where the predicted outcomes were rigorously tested through experimental evaluation. The experimental setup validated the theoretical models by demonstrating the device's stable performance under real-world conditions. The results confirmed that the system met the anticipated design requirements, ensuring the induction cooker's safety, efficiency, and long-term durability. This comprehensive approach to design, simulation, control programming, and experimental validation provided a robust framework for developing advanced induction cooking appliances with enhanced capabilities. The results show that the expected results were obtained, as seen in Table 1. The prototype performed as intended, as indicated in Section 6. In order to be used for commercial applications, the laboratory application will be converted to a company application by comparing it with industrial examples in future studies. For future research, several avenues could be explored to further enhance the performance and capabilities of induction cooking technology utilizing quasi-resonant inverters. One potential direction is the development of adaptive control algorithms that dynamically adjust the inverter's operating frequency and power output based on real-time feedback from load conditions, temperature sensors, and power consumption data. This could lead to improved energy efficiency and cooking precision, especially for varying cookware types and sizes.

Funding: This research received no external funding.

Institutional Review Board Statement: Not applicable.

Informed Consent Statement: Not applicable.

Data Availability Statement: Data is contained within the article.

Conflicts of Interest: The authors declare no conflicts of interest.

References

1. Lucia, O.; Maussion, P.; Dede, E.J.; Burdio, J.M. Induction Heating Technology and Its Applications: Past Developments, Current Technology, and Future Challenges. *IEEE Trans. Ind. Electron.* **2013**, *61*, 2509–2520. [CrossRef]
2. Serrano, J.; Lope, I.; Acero, J. Nonplanar Overlapped Inductors Applied to Domestic Induction Heating Appliances. *IEEE Trans. Ind. Electron.* **2019**, *66*, 6916–6924. [CrossRef]
3. Pascual, A.; Acero, J.; Llorente, S.; Carretero, C.; Burdio, J.M. Self-Adaptive Overtemperature Protection Materials for Safety-Centric Domestic Induction Heating Applications. *IEEE Access* **2023**, *11*, 1193–1201. [CrossRef]
4. Sarnago, H.; Burdio, J.M.; Lucia, O. High-Performance and Cost-Effective ZCS Matrix Resonant Inverter for Total Active Surface Induction Heating Appliances. *IEEE Trans. Power Electron.* **2019**, *34*, 117–125. [CrossRef]
5. Sarnago, H.; Guillen, P.; Burdio, J.M.; Lucia, O. Multiple-Output ZVS Resonant Inverter Architecture for Flexible Induction Heating Appliances. *IEEE Access* **2019**, *7*, 157046–157056. [CrossRef]
6. Serrano, J.; Acero, J.; Lope, I.; Carretero, C.; Burdio, J.M. A Flexible Cooking Zone Composed of Partially Overlapped Inductors. *IEEE Trans. Ind. Electron.* **2018**, *65*, 7762–7771. [CrossRef]
7. Jang, E.; Kwon, M.J.; Park, S.M.; Ahn, H.M.; Lee, B.K. Analysis and Design of Flexible-Surface Induction-Heating Cooktop with GaN-HEMT-Based Multiple Inverter System. *IEEE Trans. Power Electron.* **2022**, *37*, 12865–12876. [CrossRef]
8. Wang, Y.; Aksoz, A.; Geury, T.; Ozturk, S.B.; Kivanc, O.C.; Hegazy, O. A Review of Modular Multilevel Converters for Stationary Applications. *Appl. Sci.* **2020**, *10*, 7719. [CrossRef]
9. Bono-Nuez, A.; Martin-Del-Brio, B.; Bernal-Ruiz, C.; Perez-Cebolla, F.J.; Martinez-Iturbe, A.; Sanz-Gorrachategui, I. The Inductor as a Smart Sensor for Material Identification in Domestic Induction Cooking. *IEEE Sens. J.* **2018**, *18*, 2462–2470. [CrossRef]
10. Plumed, E.; Lope, I.; Acero, J. Modeling and Design of Cookware for Induction Heating Technology with Balanced Electromagnetic and Thermal Characteristics. *IEEE Access* **2022**, *10*, 83793–83801. [CrossRef]
11. Farajdadian, S.; Hajizadeh, A.; Soltani, M. Recent developments of multiport DC/DC converter topologies, control strategies, and applications: A comparative review and analysis. *Energy Rep.* **2024**, *11*, 1019–1052. [CrossRef]
12. Shakeera, S.; Rachananjali, K. Advancing Power Conversion: A Comprehensive Survey on Reduced Multilevel Inverters, Switching Techniques, and Controllers. In Proceedings of the 2024 International Conference on Advancements in Power, Communication and Intelligent Systems (APCI), Kannur, India, 21–22 June 2024; pp. 1–6.
13. Salem, M.; Richelli, A.; Yahya, K.; Hamidi, M.N.; Ang, T.Z.; Alhamrouni, I. A comprehensive review on multilevel inverters for grid-tied system applications. *Energies* **2022**, *15*, 6315. [CrossRef]
14. Chouhan, J.; Gawhade, P.; Ojha, A.; Swarnkar, P. A comprehensive review of hybrid energy systems utilizing multilevel inverters with minimal switch count. *Electr. Eng.* **2024**, 1–25. [CrossRef]
15. Rashid, M.H.; Hui, S.Y.R.; Chung, H.S.H.; Madichetty, S.; Kumar, N.S.; Krishna, B.M. Resonant and Soft-Switching Converters. In *Power Electronics Handbook*; Butterworth-Heinemann: Oxford, UK, 2024; pp. 345–405.
16. Hinov, N.; Gilev, B. Neural Network-Based Design of a Buck Zero-Voltage-Switching Quasi-Resonant DC–DC Converter. *Mathematics* **2024**, *12*, 3305. [CrossRef]
17. Sarnago, H.; Burdio, J.M.; Lucia, O. Dual-Output Extended-Power-Range Quasi-Resonant Inverter for Induction Heating Appliances. *IEEE Trans. Power Electron.* **2022**, *38*, 3385–3397. [CrossRef]
18. Yilmaz, E.N.; Aksoz, A.; Saygin, A. Design of an off-grid model of micro-smart grid connection of an asynchronous motor fed with LUO converter. *Electr. Eng.* **2018**, *100*, 2659–2666. [CrossRef]
19. Dupuy, D.; Pedreira, D.; Verbeke, D.; Leconte, V.; Wendling, P.; Rondot, L.; Mazauric, V. Adaptive Meshing for Eddy Current Calculations. *IEEE Trans. Magn.* **2015**, *51*, 7402504. [CrossRef]
20. Rehm, F.; Breining, P.; Hiller, M. Determination of Electromagnetic Material Properties of Ferromagnetic Stainless Steel Used in Domestic Induction Heating Cookware. In Proceedings of the 2022 International Conference on Electrical Machines (ICEM), Valencia, Spain, 5–8 September 2022; pp. 1009–1014. [CrossRef]
21. FisherTechnology. Eddy Current Method. Available online: https://www.helmut-fischer.com/applications/solutions/phase-sensitive-eddy-current-method (accessed on 15 July 2024).
22. Morandi, A.; Fabbri, M. In-Depth Induction Heating of Large Steel Slabs by Means of a DC Saturating Field Produced by Superconducting Coils. *IEEE Trans. Appl. Supercond.* **2016**, *26*, 0604007. [CrossRef]
23. Sorokin, D. Simulation of High-frequency Induction Heating. In Proceedings of the 2020 10th International Conference on Advanced Computer Information Technologies (ACIT), Deggendorf, Germany, 16–18 September 2020; pp. 39–42. [CrossRef]
24. Lin, C.W.; Liu, H.C.; Chang, Y.L.; Lin, Y.C.; Chen, Y.Y.; Lin, C.W.; Huang, M.S.; Hsu, H.Y. Thermal analysis of boiling pot with single coil induction cooker. In Proceedings of the 2022 21st IEEE Intersociety Conference on Thermal and Thermomechanical Phenomena in Electronic Systems (iTherm), San Diego, CA, USA, 31 May–3 June 2022; pp. 1–6. [CrossRef]
25. Kasasbeh, A.; Kelleci, B.; Ozturk, S.B.; Aksoz, A.; Hegazy, O. SEPIC Converter with an LC Regenerative Snubber for EV Applications. *Energies* **2020**, *13*, 5765. [CrossRef]
26. Kucukosman, H.; Poyrazoglu, G. Quasi-Resonant Circuitry to Improve Heat Transfer and Efficiency in Induction Cooker. In Proceedings of the 2021 17th Conference on Electrical Machines, Drives and Power Systems (ELMA), Sofia, Bulgaria, 1–4 July 2021; pp. 1–6. [CrossRef]
27. Aksoz, A.; Song, Y.; Saygin, A.; Blaabjerg, F.; Davari, P. Improving Performance of Three-Phase Slim DC-Link Drives Utilizing Virtual Positive Impedance-Based Active Damping Control. *Electronics* **2018**, *7*, 234. [CrossRef]

28. Ozturk, M.; Aslan, S.; Altintas, N.; Sinirlioglu, S. Comparison of Induction Cooker Power Converters. In Proceedings of the 2018 6th International Conference on Control Engineering & Information Technology (CEIT), Istanbul, Turkey, 25–27 October 2018; pp. 1–6. [CrossRef]
29. Lee, J.; Lim, S.; Nam, K.; Choi, D. An Optimal Selection of Induction-Heater Capacitance Considering Dissipation Loss Caused by ESR. *IEEE Trans. Ind. Appl.* **2007**, *43*, 1117–1125. [CrossRef]
30. Topuz, N.E.; Dawood, K.; Kaya, U.; Odabas, G.; Komurgoz, G. Electromagnetic and Thermal Analysis of a Domestic Induction Cooker Coil. In Proceedings of the 2019 4th International Conference on Power Electronics and their Applications (ICPEA), Elazig, Turkey, 25–27 September 2019; pp. 1–5. [CrossRef]
31. Kaizer Power Electronics. Spiral Coil Inductance Estimation. Available online: https://kaizerpowerelectronics.dk/calculators/spiral-coil-calculator/ (accessed on 31 October 2024).
32. Tong, Q.; Huang, C. A design for coil disk of induction cooker with integrated magnetic coil skeleton. In Proceedings of the 2017 IEEE 2nd Information Technology, Networking, Electronic and Automation Control Conference (ITNEC), Chengdu, China, 15–17 December 2017; pp. 673–676. [CrossRef]
33. Jones, G.; Rogers, D. Investigation of IGBT switching energy loss and peak overvoltage using digital active gate drives. In Proceedings of the 2017 IEEE 18th Workshop on Control and Modeling for Power Electronics (COMPEL), Stanford, CA, USA, 9–12 July 2017; pp. 1–8. [CrossRef]
34. TOSHIBA. TLP250. Available online: https://toshiba.semicon-storage.com/info/docget.jsp?did=16821 (accessed on 31 October 2024).
35. Manuel, A.; Gopinath, D. A simulation study of SiC MOSFET characteristics and design of gate drive card using TLP250. In Proceedings of the 2016 International Conference on Next Generation Intelligent Systems (ICNGIS), Kottayam, India, 1–3 September 2016; pp. 1–5. [CrossRef]
36. Latina, M.A.E.; Sejera, M.P.; Mitra, J.P.V.; Monton, B.S.; Pundan, C.S. A Study of the Effect of Integrating Low-Pass Filter in Measuring the Dynamic Performance of a High Speed 8-bit Analog-to-Digital Converter (ADC). In Proceedings of the 2018 IEEE 10th International Conference on Humanoid, Nanotechnology, Information Technology, Communication and Control, Environment and Management (HNICEM), Baguio City, Philippines, 29 November–2 December 2018; pp. 1–6. [CrossRef]
37. STMicroelectronic. STM32F103x8. Available online: https://www.st.com/resource/en/datasheet/stm32f103cb.pdf (accessed on 31 October 2024).
38. Ozturk, M.; Oktay, U.; Yilmaz, N.; Yardibi, H.S.; Sinirlioglu, S. Comparison of Pan Detection Methods for Single Switch Topology Used in Domestic Induction Cooking. In Proceedings of the 2020 International Conference on Smart Energy Systems and Technologies (SEST), Istanbul, Turkey, 7–9 September 2020; pp. 1–6. [CrossRef]
39. See, K.Y.; Bullo, M.; Dughiero, F.; Sieni, E. Practical papers, articles and application notes. *IEEE Electromagn. Compat. Mag.* **2013**, *2*, 49–58. [CrossRef]
40. Lim, G.-S.; Kim, W.-M.; Cho, Y.-K.; Lee, S.-W. Quasi-Resonant Fly-Buck Converter with Active Switching for Improved Output Voltage Boosting and Regulation. *IEEE Trans. Ind. Electron.* **2024**, *71*, 12153–12164. [CrossRef]
41. Altintas, N.; Ozturk, M.; Oktay, U. Performance evaluation of pan position methods in domestic induction cooktops. *Electr. Eng.* **2023**, *105*, 2559–2571. [CrossRef]
42. Ozturk, M.; Altintas, N. Multi-output AC–AC converter for domestic induction heating. *Electr. Eng.* **2023**, *105*, 297–316. [CrossRef]
43. Salvi, B.; Porpandiselvi, S.; Vishwanathan, N. An Inverter Circuit Configuration Suitable for Vessels of Different Material for Multiload Induction Cooking Application. *IEEE J. Emerg. Sel. Top. Power Electron.* **2023**, *11*, 3223–3235. [CrossRef]
44. Hsieh, H.; Kuo, C.; Chang, W. Study of half-bridge series-resonant induction cooker powered by line rectified DC with less filtering. *IET Power Electron.* **2023**, *16*, 1929–1942. [CrossRef]
45. Xu, X.; Chen, Q.; Ke, G.; Xu, L.; Ren, X.; Zhang, Z. A Flat-Top Single-Ended Resonant Converter with Low Switch Voltage Stress. *IEEE Trans. Power Electron.* **2023**, *38*, 11673–11684. [CrossRef]
46. Wang, Y.; Li, M. Establishment and Verification of Core Loss Model of Nanocrystalline under Square Wave Excitation. In Proceedings of the ISMSEE 2022—The 2nd International Symposium on Mechanical Systems and Electronic Engineering, Zhuhai, China, 25–27 February 2022; pp. 1–6.
47. Sanusi, B.N.; Ouyang, Z. Integrated inductor design for a highly compact embedded battery charger. *IEEE Trans. Power Electron.* **2022**, *37*, 8873–8885. [CrossRef]
48. Roberto, S.F.; Sciré, D.; Lullo, G.; Vitale, G. Equivalent circuit modelling of ferrite inductors losses. In Proceedings of the 2018 IEEE 4th International Forum on Research and Technology for Society and Industry (RTSI), Palermo, Italy, 10–13 September 2018; pp. 1–4.